Polarization test of gravitational waves from compact binary coalescences

Hiroki Takeda,[1,*] Atsushi Nishizawa,[2] Yuta Michimura,[1] Koji Nagano,[3] Kentaro Komori,[1] Masaki Ando,[1] and Kazuhiro Hayama[4]

[1]*Department of Physics, University of Tokyo, Bunkyo, Tokyo 113-0033, Japan*
[2]*Kobayashi-Maskawa Institute for the Origin of Particles and the Universe, Nagoya University, Nagoya, Aichi 464-8602, Japan*
[3]*KAGRA Observatory, Institute for Cosmic Ray Research, University of Tokyo, Kashiwa, Chiba 277-8582, Japan*
[4]*Department of Applied Physics, Fukuoka University, Nanakuma, Fukuoka 814-0180, Japan*

(Received 18 June 2018; published 12 July 2018)

Gravitational waves have only two polarization modes in general relativity. However, there are six possible modes of polarization in a generic metric theory of gravity. Thus, tests of gravitational-wave polarization can be tools for pursuing the nature of space-time structure. The observations of gravitational waves with a worldwide network of interferometric detectors such as Advanced LIGO, Advanced Virgo, and KAGRA will make it possible to obtain the information of gravitational-wave polarization from detector signals. We study the separability of the polarization modes for the inspiral gravitational waves from the compact binary coalescences systematically. Unlike some other waveforms such as burst, the binary parameters need to be properly considered. We show that three polarization modes of gravitational waves would be separable with the global network of three detectors to some extent, depending on the signal-to-noise ratio and the duration of the signal. We also show that with four detectors the three polarization modes would be more easily distinguished by breaking a degeneracy of the polarization modes and even the four polarization modes would be separable.

DOI: 10.1103/PhysRevD.98.022008

I. INTRODUCTION

The first detection of gravitational waves (GWs) from binary black holes (BBH) by Advanced LIGO (aLIGO) [1] marked the dawn of the new field of gravitational-wave astronomy [2]. Soon after, the observations of GWs by aLIGO and Advanced Virgo (AdV) [3] enabled some experimental studies to probe into the nature of gravity [4,5].

The accurate information on GW modes is expected to improve our understanding of gravity. Polarizations of null GWs can be treated by the Newman-Penrose formalism strictly and transparently [6,7]. In general relativity (GR), a GW has two polarization modes (plus and cross modes, which are tensor modes). However, a general metric theory allows GWs to have at most six polarizations: two tensor modes (plus, cross), two vector modes (vector x, vector y), and two scalar modes(breathing, longitudinal) [8,9]. In modified gravity theories such as scalar-tensor theory [10] and $f(R)$ gravity [11], scalar polarizations are allowed in addition to tensor modes. In contrast, up to six polarizations are allowed in bimetric gravity theory [12], while up to five polarizations are allowed in massive gravity theory [13]. If nontensorial polarization modes are found by the observations of GWs, it indicates that an alternative to GR should exist as a fundamental theory and the theory of gravity should be extended beyond GR. Therefore, the test of gravitational-wave polarizations can be a powerful tools for pursuing the nature of space-time structure.

In principle, the number of the detectors needs to be equal to the number of the polarization modes of the GW to separate the modes. In the near future, KAGRA [14–17], a laser interferometric detector being developed at the Kamioka mine in Japan, and LIGO India will participate in the global network as the fourth and fifth detectors. Therefore, more polarization modes can soon be probed with the larger number of detectors.

Some analytical attempts to separate the polarization modes were made for GW bursts [18], stochastic GWs [19], and continuous GWs [20]. However, it is more difficult to analyze in the case of compact binary coalescences (CBCs) because the waveforms of the gravitational waves from CBCs have the source model parameters, which determine the frequency evolution in time and are correlated with each other. We focus especially on the polarization modes of the inspiral GW from CBCs. A simple data analysis method using the simple sine-Gaussian wave packet waveform as a toy model to probe gravitational-wave polarization from

*takeda@granite.phys.s.u-tokyo.ac.jp

CBCs was reported [21,22]. Also, a polarization mode search of GW170814 had already been conducted [23]. However, only a simplistic analysis involving the substitution of the antenna pattern functions was done. Since the observational limitation on the polarization modes may change depending on the inclination-angle dependence and the existence of other polarization modes besides the antenna patterns for each polarization modes, these dependences need to be properly considered.

It is necessary to gain a better understanding of the correlations and degeneracies among the parameters in a realistic waveform of CBCs to separate and reconstruct the polarization modes in the presence of nontensorial polarization modes. We study parameter estimation errors and the correlations between parameters in the presence of nontensorial polarizations in addition to tensor modes with global detector networks systematically.

This paper is organized as follows. In Sec. II, we describe polarization modes of gravitational waves, antenna pattern functions, and detector signal. In Sec. III, we explain the angular dependence of a gravitational waveform in modified gravity and introduce the polarization models adopted in our analysis. In Sec. IV, we go through the basics of Fisher analysis and introduce the our numerical setup. In Sec. V, we show the results of our parameter estimation in the presence of nontensorial polarization modes. We devote the last section, Sec. VII, to the conclusion of this paper.

II. ANTENNA PATTERN FUNCTIONS

A. Polarization mode of gravitational waves

In general, there are six possible modes of polarization in a metric gravity theory [8,9]. At any given space-time point, GW metric perturbations can be expressed as

$$h_{ab}(t,\hat{\Omega}) = h_A(t)e^A_{ab}(\hat{\Omega}), \tag{1}$$

where $\hat{\Omega}$ is the sky direction of a GW source and $A = +,\times,x,y,b,l$ are the polarization indices and are referred to as plus, cross, vector x, vector y, breathing, and longitudinal, respectively. $e^A_{ab}(\hat{\Omega})$ are polarization tensors defined by

$$e^+_{ab} = \hat{e}_x \otimes \hat{e}_x - \hat{e}_y \otimes \hat{e}_y, \tag{2}$$

$$e^\times_{ab} = \hat{e}_x \otimes \hat{e}_y + \hat{e}_y \otimes \hat{e}_x, \tag{3}$$

$$e^x_{ab} = \hat{e}_x \otimes \hat{e}_z + \hat{e}_z \otimes \hat{e}_x, \tag{4}$$

$$e^y_{ab} = \hat{e}_y \otimes \hat{e}_z + \hat{e}_z \otimes \hat{e}_y, \tag{5}$$

$$e^b_{ab} = \hat{e}_x \otimes \hat{e}_x + \hat{e}_y \otimes \hat{e}_y, \tag{6}$$

$$e^l_{ab} = \sqrt{2}\hat{e}_z \otimes \hat{e}_z, \tag{7}$$

where the set of unit vectors $\{\hat{e}_x,\hat{e}_y,\hat{e}_z\}$ forms the wave orthonormal coordinate such that $\hat{e}_z = -\hat{\Omega}$ is a unit vector in the direction of propagation of the GW and $\hat{e}_z = \hat{e}_x \times \hat{e}_y$. We have a degree of freedom (d.o.f.) of choice for $\hat{e}_x,\hat{e}_y$ around the $\hat{e}_z$ axis. This d.o.f. is referred to as the polarization angle ψ_p.

B. Antenna pattern functions and detector signal

The detector signal of the Ith detector is given by [18,19,24]

$$h_I(t,\hat{\Omega}) = d^{ab}_I h_{ab}(t) = F^A_I(\hat{\Omega})h_A(t). \tag{8}$$

Here, d_I is the detector tensor defined by

$$d_I \coloneqq \frac{1}{2}(\hat{u}_I \otimes \hat{u}_I - \hat{v}_I \otimes \hat{v}_I), \tag{9}$$

where $\hat{u}_I$ and $\hat{v}_I$ are unit vectors along with arms of the Ith interferometric detector. F^A_I is the antenna pattern functions of the Ith detector for polarization A defined by

$$F^A_I(\hat{\Omega}) \coloneqq d^{ab}_I e^A_{ab}(\hat{\Omega}). \tag{10}$$

The specific formulas of the antenna pattern are provided in Ref. [19]. We note that the above expressions are correct when the length of the interferometer arm is much smaller than the wavelength of the observed GW. This condition is satisfied for ground-based detectors such as aLIGO, AdV, and KAGRA.

III. POLARIZATIONS

A. Angular dependence of a GW waveform in modified gravity

The waveform of GW [$h_A(t)$ in Eq. (8)] depends on the inclination angle ι of a compact binary orbit as we will show below. In GR where only tensor modes are admitted, the signal including the angular parameters (inclination angle, source position angles, and detector position angles) and antenna pattern functions of the Ith detector is

$$h_I = \frac{2}{5}\mathcal{G}_{T,I}h_{\rm GR}, \tag{11}$$

where $h_{\rm GR}$ corresponds to the GW waveform predicted by GR. Specifically, $h_{\rm GR}$ is the Fourier component of the amplitude h_+ in Eq. (1) in the direction perpendicular to the binary orbital plane. Here, $\mathcal{G}_{T,I}$ is the geometrical factor for the tensor mode for the Ith detector, defined by

$$\mathcal{G}_{T,I} \coloneqq \frac{5}{2}\{(1+\cos^2\iota)F_{+,I}(\boldsymbol{\theta_s},\boldsymbol{\theta_e}) + 2i\cos\iota F_{\times,I}(\boldsymbol{\theta_s},\boldsymbol{\theta_e})\} \times e^{i\phi_{D,I}(\theta_s,\phi_s,\theta_e,\phi_e)}, \tag{12}$$

where $\boldsymbol{\theta_s} \coloneqq (\theta_s, \phi_s, \psi_p)$ is the source direction angle parameters (θ_s, ϕ_s) and polarization angle ψ_p, $\boldsymbol{\theta_e} \coloneqq (\theta_e, \phi_e, \psi)$ is the detector location and orientation angle parameters, and $\phi_{D,I}$ is the Doppler phase for the Ith detector [25,26]. The factor of $2/5$ in Eq. (11) appears so that the angular average of Eq. (12) gives unity.

The antenna pattern functions for nontensorial modes are defined in Eq. (10). However, when we discuss the problem of the separation of polarization modes, we need to consider the inclination-angle dependence for scalar modes and vector modes, which is fixed by the geometry of the binary stellar system. Metric perturbations of GWs are given by the quadrupole formula

$$h_{ab}(t, \boldsymbol{x}) = \frac{1}{r}\frac{2G}{c^4}\ddot{M}_{ab}(t - r/c), \tag{13}$$

where M_{ab} is the moment of a mass distribution. a and b run over 1, 2, and 3, which correspond to the source coordinate $\{x_1, x_2, x_3\}$ such that the binary circular motion is included in the x_1–x_2 plane. In GR, transverse-traceless projection for M_{ab} can fix the gauge freedom [27]. As a result, plus and cross tensor modes are only admitted. In modified gravity, the gauge symmetry is not held, leading to additional d.o.f. for GW. Therefore, nontensorial modes are obtained by keeping non–transverse traceless modes. According to Eq. (1), the nontensorial polarization modes of GW propagating in the direction (along coordinate 3) perpendicular to the orbital plane are

$$h_x(t) = \frac{1}{r}\frac{2G}{c^4}\ddot{M}_{13}(t - r/c), \tag{14}$$

$$h_y(t) = \frac{1}{r}\frac{2G}{c^4}\ddot{M}_{23}(t - r/c), \tag{15}$$

$$h_b(t) = \frac{1}{r}\frac{G}{c^4}(\ddot{M}_{11}(t - r/c) + \ddot{M}_{22}(t - r/c)), \tag{16}$$

$$h_l(t) = \frac{1}{r}\frac{\sqrt{2}G}{c^4}\ddot{M}_{33}(t - r/c). \tag{17}$$

For a GW propagating in the direction of $\hat{n} = (\sin\iota\cos\phi, \sin\iota\sin\phi, \cos\iota)$, the expression of the amplitude can be obtained by rotating M_{ab} in the above expressions.

For a circular binary star system moving with

$$\begin{aligned} x_1(t) &= R\cos(\omega_s t + \pi/2), \\ x_2(t) &= R\sin(\omega_s t + \pi/2), \\ x_3(t) &= 0, \end{aligned} \tag{18}$$

the second time derivatives of the mass moments are

$$\ddot{M}_{11} = -\ddot{M}_{22} = 2\mu R^2\omega_s^2\cos 2\omega_s t, \tag{19}$$

$$\ddot{M}_{12} = 2\mu R^2\omega_s^2\sin 2\omega_s t, \tag{20}$$

where ω_s, μ, and R are the angular frequency of the binary stars, the reduced mass, and the orbital radius, respectively.

Finally, we can get the simple expressions about the amplitudes for nontensorial polarization modes

$$h_x = -\frac{4G\mu\omega_s^2R^2}{rc^4}\frac{\sin 2\iota}{2}\cos(2\omega_s t_{\rm ret} + 2\phi), \tag{21}$$

$$h_y = -\frac{4G\mu\omega_s^2R^2}{rc^4}\sin\iota\sin(2\omega_s t_{\rm ret} + 2\phi), \tag{22}$$

$$h_b = -\frac{4G\mu\omega_s^2R^2}{rc^4}\frac{\sin^2\iota}{2}\cos(2\omega_s t_{\rm ret} + 2\phi), \tag{23}$$

$$h_l = \frac{4G\mu\omega_s^2R^2}{rc^4}\frac{\sin^2\iota}{\sqrt{2}}\cos(2\omega_s t_{\rm ret} + 2\phi), \tag{24}$$

where $t_{\rm ret}$ is the retarded time defined by $t_{\rm ret} = t - r/c$.

From these expressions, we define the geometrical factors for vector modes (V_x, V_y) and scalar modes(S_2), including the inclination-angle dependence, as follows:

$$\mathcal{G}_{V_x,I} \coloneqq \sqrt{\frac{525}{56}}\sin 2\iota F_{V_x,I}(\boldsymbol{\theta_s}, \boldsymbol{\theta_e})e^{i\phi_{D,I}(\theta_s,\phi_s,\theta_e,\phi_e)}, \tag{25}$$

$$\mathcal{G}_{V_y,I} \coloneqq \sqrt{\frac{15}{2}}\sin\iota F_{V_y,I}(\boldsymbol{\theta_s}, \boldsymbol{\theta_e})e^{i\phi_{D,I}(\theta_s,\phi_s,\theta_e,\phi_e)}, \tag{26}$$

$$\mathcal{G}_{S_2,I} \coloneqq \sqrt{\frac{225}{8}}\sin^2\iota F_{b,I}(\boldsymbol{\theta_s}, \boldsymbol{\theta_e})e^{i\phi_{D,I}(\theta_s,\phi_s,\theta_e,\phi_e)}. \tag{27}$$

In addition to the above geometrical factors, the scalar dipole radiation may exist in modified gravity theories with a scalar d.o.f. For a circular binary motion, the monopole radiation of the scalar mode vanishes, and the dominant radiation of the scalar mode in the early inspiral phase can be dipole radiation. The dependence on the inclination angle is proportional to $\sin\iota$, which is the result in the case of Brans-Dicke theory obtained by Ref. [28]. Thereby, we define the geometrical factor for the scalar dipole radiation as

$$\mathcal{G}_{S_1,I} \coloneqq \sqrt{\frac{45}{2}}\sin\iota F_{b,I}(\boldsymbol{\theta_s}, \boldsymbol{\theta_e})e^{i\phi_{D,I}(\theta_s,\phi_s,\theta_e,\phi_e)}. \tag{28}$$

These geometrical factors are normalized by the angular average over the whole sky and the inclination angle as well as Eq. (12).

B. Polarization models

Here, we summarize the polarization models used in our analysis. We assume the waveforms of nontensorial polarization modes are the same as those of tensor modes $h_{\rm GR}$ in Eq. (11), although these waveforms actually depend on the specific theory of gravity. In other words, we consider pessimistic cases in terms of separating

polarization modes because it is more difficult to separate modes having the same waveforms.

Model T: General relativity model The model T general relativity model is a pure GR model. Thereby, no additional polarization parameters are taken into account,

$$h_I = \mathcal{G}_{T,I} h_{\rm GR}. \tag{29}$$

Model TS1: Tensor-scalar dipole model In the tensor-scalar dipole model, we add a scalar mode having the inclination-angle dependence of dipole radiation. Thus, the additional model parameter is the scalar mode amplitude A_{S_1}. We use the frequency evolution of the tensor modes for the dipole radiation because our purpose is to check the effect of the inclination-angle dependence of the geometrical factor here. Since a specific waveform of dipole radiation depends on the theory used, further investigation is needed,

$$h_I = \{\mathcal{G}_{T,I} + A_{S_1}\mathcal{G}_{S_1,I}\} h_{\rm GR}. \tag{30}$$

Model TS2: Tensor-scalar quadrupole model In the tensor-scalar quadrupole model, we add a scalar mode having the inclination-angle dependence of quadrupole radiation. Thus, the additional model parameter is the scalar mode amplitude A_{S_2},

$$h_I = \{\mathcal{G}_{T,I} + A_{S_2}\mathcal{G}_{S_2,I}\} h_{\rm GR}. \tag{31}$$

Model TVxS2: Tensor-scalar quadrupole and vector x model In the tensor-scalar quadrupole and vector x model, we add the combination of the scalar mode having the inclination-angle dependence of quadrupole radiation and the vector x mode. The additional model parameters are thus the amplitudes (A_{S_2}, A_{V_x}),

$$h_I = \{\mathcal{G}_{T,I} + A_{S_2}\mathcal{G}_{S_2,I} + A_{V_x}\mathcal{G}_{V_x,I}\} h_{\rm GR}. \tag{32}$$

Model TVyS1: Tensor-scalar dipole and vector y model In the tensor-scalar dipole and vector y model, we add the combination of the scalar mode having the inclination-angle dependence of dipole radiation and the vector y mode. The additional model parameters are the amplitudes (A_{S_1}, A_{V_y}). It is assumed that it is more difficult to separate modes S_2 and A_{V_x} than other combinations because these modes have the same inclination dependence of the geometrical factors. Thus, we choose this combination as a pessimistic case,

$$h_I = \{\mathcal{G}_{T,I} + A_{S_1}\mathcal{G}_{S_1,I} + A_{V_y}\mathcal{G}_{V_y,I}\} h_{\rm GR}. \tag{33}$$

Model TV: Tensor vector model In the tensor vector model, we add the combination of the vector x and vector y modes. The additional model parameters are the amplitudes (A_{V_x}, A_{V_y}),

$$h_I = \{\mathcal{G}_{T,I} + A_{V_x}\mathcal{G}_{V_x,I} + A_{V_y}\mathcal{G}_{V_y,I}\} h_{\rm GR}. \tag{34}$$

IV. SETUP

A. Fisher analysis

The model parameter estimation can be evaluated by a Fisher information matrix [25,29,30]. The Fisher information matrix Γ is given by

$$\Gamma_{ij} \coloneqq 4{\rm Re}\int_{f_{\rm min}}^{f_{\rm max}} df \sum_I \frac{1}{S_{n,I}(f)} \frac{\partial h_I^*(f)}{\partial \lambda^i} \frac{\partial h_I(f)}{\partial \lambda^j}, \tag{35}$$

where $S_{n,I}(f)$ is the Ith detector noise power spectrum and λ_i is the ith parameter. The root mean square of a parameter and the correlation coefficient between two parameters can be calculated using the inverse of the Fisher information matrix. The root mean square of $\Delta\lambda^i$ is defined by

$$(\Delta\lambda_i)_{\rm rms} \coloneqq \sqrt{\langle \Delta\lambda^i \Delta\lambda^i \rangle} = \sqrt{(\Gamma^{-1})^{ii}}, \tag{36}$$

and the correlation coefficient between λ_i, λ_j is calculated by

$$C(\lambda_i, \lambda_j) \coloneqq \frac{\langle \Delta\lambda^i \Delta\lambda^j \rangle}{\langle (\Delta\lambda_i)^2 \rangle \langle (\Delta\lambda_j)^2 \rangle} = \frac{(\Gamma^{-1})^{ij}}{\sqrt{|(\Gamma^{-1})^{ii}(\Gamma^{-1})^{jj}|}}, \tag{37}$$

where $\Delta\lambda^i$ is the measurement error of λ^i and $\langle\cdot\rangle$ stands for the ensemble average. The sky localization error, the error in the solid angle (measured in steradians), is defined by

$$\Delta\Omega_s \coloneqq 2\pi |\sin\theta_s| \sqrt{\langle (\Delta\theta_s)^2 \rangle \langle (\Delta\phi_s)^2 \rangle - \langle \Delta\theta_s \Delta\phi_s \rangle^2}. \tag{38}$$

Hereafter, we simply refer to $(\Delta\lambda_i)_{\rm rms}$ as $\Delta\lambda_i$ and call it the estimation error of λ_i.

B. Analytical and numerical setup

We use the following inspiral waveform up to 3 post-Newtonian order (PN order) in amplitude and 3.5 PN order in phase,

$$h_{\rm GR} = A_{\rm ins} e^{-i\phi_{\rm ins}}, \tag{39}$$

with

$$A_{\rm ins} = \frac{1}{\sqrt{6}\pi^{2/3} d_L} \mathcal{M}^{5/6} f^{-7/6} \sum_{i=0}^{6} (\pi\mathcal{M}f)^{i/3}, \tag{40}$$

$$\phi_{\rm ins} = 2\pi f t_c - \phi_c - \frac{\pi}{4} + \frac{3}{128}(\pi\mathcal{M}f)^{-5/3} \sum_{i=0}^{7} \phi_i (\pi\mathcal{M}f)^{i/3}, \tag{41}$$

as a waveform of inspiral GW, compiled in Ref. [31]. Here, $\mathcal{M}$ is the chirp mass, d_L is the luminosity distance, t_c is the coalescence time, and ϕ_c is the phase at the coalescence time. We set the lower-frequency end of various integration to be $f_{\rm min} = 30$ Hz and the upper-frequency end $f_{\rm max}$ to be the frequency $f_{\rm ISCO}$ that is twice the innermost stable circular orbit frequency for a point mass in Schwarzschild space-time

TABLE I. Medians of parameter estimation errors and their correlation coefficients. Masses of BBHs and BNSs are $10\ M_\odot - 10\ M_\odot$ and $1.4\ M_\odot - 1.4\ M_\odot$, respectively. Only correlation coefficients larger than 10% are shown. The improvement factor is defined by the ratio of the error with HLV to the error with HLVK. We say that the polarization modes would be separable when the errors of the amplitudes parameter are less than unity. The two conditions for the separation of polarization modes are breaking the degeneracy among polarization modes by enough detectors and reducing the errors of the amplitude parameters from another practical point of view, for example, the SNR and the duration of the signal.

	Parameter	BBH (HLV)	BBH (HLVK)	Improvement factor	BNS (HLV)	BNS (HLVK)	Improvement factor
ModelT	SNR	33.3	40.2		36.4	44.3	
	$\Delta \ln d_L$	0.269	0.137	1.96	0.183	0.107	1.71
	$\Delta\Omega_s$ (deg^2)	5.91	1.77	3.34	1.39	0.517	2.69
ModelTS1	$\Delta \ln d_L$	0.678	0.179	3.79	0.359	0.134	2.68
	$\Delta\Omega_s$ (deg^2)	4.74	0.912	5.20	0.919	0.250	3.68
	ΔA_{S1}	1.16	0.284	4.08	0.606	0.197	3.08
	$C(A_{S1}, \log d_L)$	0.998	0.989		0.996	0.984	
	$C(A_{S1}, \cos\iota)$	−0.553	−0.500		−0.231	−0.159	
ModelTS2	$\Delta \ln d_L$	0.676	0.182	3.71	0.358	0.134	2.67
	$\Delta\Omega_s$ (deg^2)	4.74	0.913	5.09	0.862	0.246	3.50
	ΔA_{S2}	1.51	0.385	3.92	0.765	0.256	2.99
	$C(A_{S2}, \log d_L)$	0.997	0.989		0.996	0.984	
	$C(A_{S2}, \cos\iota)$	−0.609	−0.564		−0.246	−0.189	
ModelTVxS2	$\Delta \ln d_L$	1.58	0.258	6.12	1.05	0.190	5.53
	$\Delta\Omega_s$ (deg^2)	6.13	0.885	6.92	0.783	0.179	4.37
	ΔA_{S2}	4.15	0.486	8.54	2.48	0.340	7.29
	ΔA_{V_x}	2.23	0.399	5.59	1.24	0.228	5.44
	$C(A_{V_x}, \log d_L)$	0.945	0.690		0.901	0.633	
	$C(A_{V_x}, \cos\iota)$	0.412	0.360		−0.189	−0.072	
	$C(A_{V_x}, A_{S2})$	0.919	0.576		0.828	0.557	
ModelTVyS1	$\Delta \ln d_L$	1.69	0.253	6.68	1.05	0.183	5.74
	$\Delta\Omega_s$ (deg^2)	6.76	0.879	7.69	0.831	0.187	4.44
	ΔA_{S1}	3.72	0.383	9.71	1.81	0.273	6.63
	ΔA_{V_y}	3.12	0.389	8.02	1.75	0.270	6.48
	$C(A_{V_y}, \log d_L)$	0.996	0.990		0.997	0.986	
	$C(A_{V_y}, \cos\iota)$	−0.660	−0.322		−0.446	−0.010	
	$C(A_{V_y}, A_{S1})$	0.996	0.983		0.996	0.982	
ModelTV	$\Delta \ln d_L$	1.98	0.310	6.39	1.22	0.193	6.32
	$\Delta\Omega_s$ (deg^2)	5.68	0.795	7.14	0.813	0.187	4.35
	ΔA_{V_x}	2.55	0.420	6.07	1.37	0.241	5.68
	ΔA_{V_y}	3.91	0.513	7.62	2.12	0.298	7.11
	$C(A_{V_y}, \log d_L)$	0.999	0.993		0.998	0.991	
	$C(A_{V_y}, \cos\iota)$	−0.846	−0.335		−0.307	−0.207	
	$C(A_{V_x}, A_{V_y})$	0.987	0.814		0.948	0.624	

$$f_{\rm ISCO} = (6^{3/2}\pi M_{\rm tot})^{-1} \simeq 0.0217 M_{\rm tot}^{-1}, \quad (42)$$

where $M_{\rm tot} = m_1 + m_2$ is the binary total mass.

We consider 11 model parameters in GR,

$$(\log\mathcal{M}, \log\eta, t_c, \phi_c, \log d_L, \chi_s, \chi_a, \theta_s, \phi_s, \cos\iota, \psi_p), \quad (43)$$

and additional polarization amplitude parameters, for example, A_{S_1} in the case of model TS1. We assume that the fiducial values of the additional amplitude parameters are 1 in all models. Here, $\log\eta$, χ_s, and χ_a are the logarithm of the mass ratio, the symmetric spin parameter, and the antisymmetric parameter, respectively. We assume that the fiducial values of t_c, ϕ_c, χ_s, and χ_a are 0 in all models. We impose the priors for parameters defined over the specific range: $\log\eta$, ϕ_c, angular parameters (θ_s, ϕ_s, $\cos\iota$, and ψ_p), and spin parameters of binary compact stars (χ_s and χ_a).

We estimate model parameters for BBHs with equal 10 $M_\odot$ masses at $z = 0.05$ and for binary neutron stars (BNSs) with equal 1.4 $M_\odot$ masses at $z = 0.01$ in each polarization model. A network total signal-to-noise ratio (SNR) > 8 is required for all sources, and angular parameters ($\cos\theta_s$, ϕ_s, $\cos\iota$, and ψ_p) are uniformly random. The number of sources calculated by Fisher analysis for one model is 500.

We consider two kinds of global networks, the first being composed of the two aLIGOs at Hanford and Livingston and AdV(HLV) and the second being HLV with KAGRA(HLVK). aLIGOs and KAGRA are assumed to have their design sensitivity [32]. AdV is assumed to have its binary neutron star optimized sensitivity [32].

We estimate model parameters in the case of BBHs or BNSs, with a detector network such as aLIGO-AdV (HLV) or aLIGO-AdV-KAGRA(HLVK) for each polarization model.

V. RESULTS

Our Fisher analysis results are shown in Table I. We show the medians of parameter estimation errors of the luminosity distance, the sky localization, and the additional polarization amplitude for each model. We also show the medians of correlation coefficients larger than 10% between the additional polarization amplitude and other parameters. In all models, the amplitude parameters of nontensorial polarization modes highly correlate with other amplitude parameters, $\ln d_L$ and $\cos\iota$.

The histograms of the parameter estimation errors in the model T for the luminosity distance, the sky localization, the inclination angle, and the polarization angle are shown in Fig. 1. In model T, the errors are reduced by adding a fourth detector, KAGRA. The error of the luminosity distance $\ln d_L$ is reduced by about a factor of 2, and the sky localization error Ω_s is also reduced by about a factor of 3. The other errors of the amplitude parameters, $\cos\iota$ and ψ_p, are also reduced by the fourth detector.

The histograms of the parameter estimation errors in the model TS1 for the luminosity distance, the sky localization, the inclination angle, the polarization angle, and the additional polarization amplitude are shown in Fig. 2. It is shown that the observation by the global network with four detectors can break a degeneracy among amplitude parameters. In the case of the model TS1, the errors of the amplitude parameters are reduced further by adding the fourth detector, KAGRA, than in the case of model T. For BNSs, A_s is determined even by three detectors, HLV. However, for BBHs, it is difficult to separate the additional polarization mode. The error is much reduced by adding the fourth detector, KAGRA. This suggests that in the case of BBHs a four-detector global network is necessary to determine the mode, though, in principle, three detectors can distinguish an additional scalar mode. The reason for

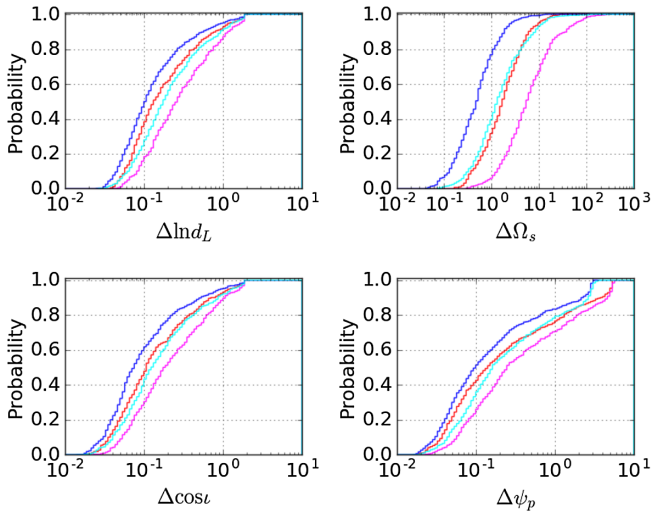

FIG. 1. Parameter estimation errors in the waveform model T. The colors are 10 $M_\odot$ − 10 $M_\odot$ with HLV (magenta), 10 $M_\odot$ − 10 $M_\odot$ with HLVK (red), 1.4 $M_\odot$ − 1.4 $M_\odot$ with HLV (cyan), and 1.4 $M_\odot$ − 1.4 $M_\odot$ with HLVK (blue). The reason for the rapid change of $\Delta\psi_p$ at around 3 is because we impose the priors for parameters having the range, angular parameters, and spin parameters of binary compact stars.

the difference from the BNS case is because the signal of BBHs is shorter than the signal of BNSs. This results in the worse estimation error of the chirp mass, which is determined mainly from the phase of the signal. Indeed, $\Delta\ln\mathcal{M} = 0.0019$ (median) in the case of BBHs, but $\Delta\ln\mathcal{M} = 0.00015$ (median) in the case of BNSs with HLV. Since the chirp mass is also included in the GW amplitude, it results in the worse parameter estimation of the amplitude in the case of BBHs. As for HLVK, $\Delta\ln\mathcal{M} = 0.0017$ (median) in

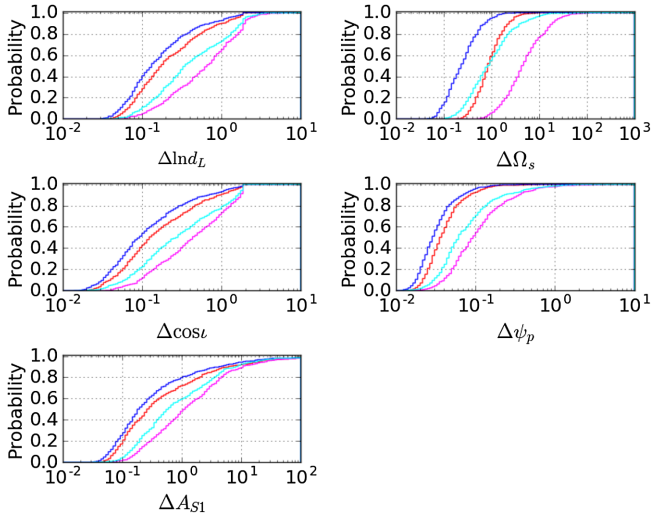

FIG. 2. Parameter estimation errors in the waveform model TS1. The colors are 10 $M_\odot$ − 10 $M_\odot$ with HLV (magenta), 10 $M_\odot$ − 10 $M_\odot$ with HLVK (red), 1.4 $M_\odot$ − 1.4 $M_\odot$ with HLV (cyan), and 1.4 $M_\odot$ − 1.4 $M_\odot$ with HLVK (blue).

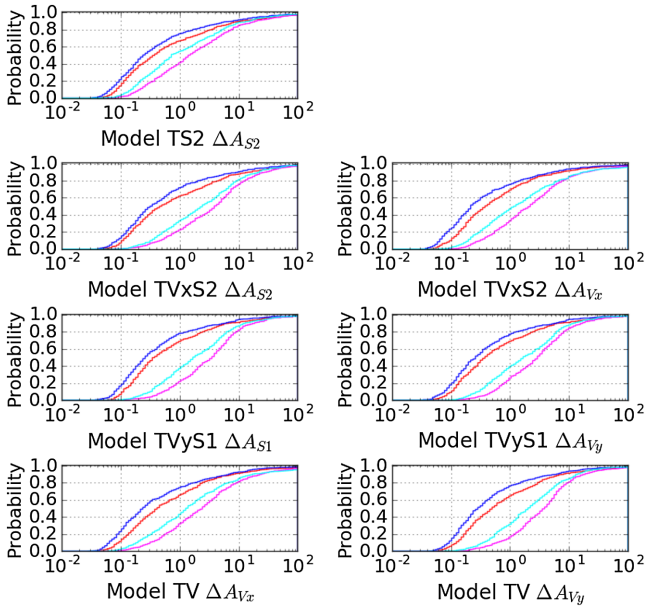

FIG. 3. Parameter estimation errors of the additional polarization amplitudes assumed as 1 for all models. The colors are $10\ M_\odot - 10\ M_\odot$ with HLV (magenta), $10\ M_\odot - 10\ M_\odot$ with HLVK (red), $1.4\ M_\odot - 1.4\ M_\odot$ with HLV (cyan), and $1.4\ M_\odot - 1.4\ M_\odot$ with HLVK (blue).

the case of BBHs, but $\Delta \ln \mathcal{M} = 0.00014$ (median) in the case of BNSs. $\Delta \ln \mathcal{M}$ for BBHs is improved by 11%, while $\Delta \ln \mathcal{M}$ for BNSs is improved by 7%.

In the case of model TS2, the errors and correlations behave the same way as in the case of model TS1.

Our results of parameter estimation for the additional polarization amplitudes in other polarization models are shown in Fig. 3. In models TVxS2, TVyS1, and TV, the errors of the amplitude parameters are larger than 1 with HLV for both BBHs and BNSs as shown in Table I, so four detectors are always necessary to determine two additional polarizations. In these cases, the errors of the additional polarization modes are reduced further by adding the fourth detector, KAGRA, than in the case of model TS1 and model TS2. In all of these models, the error is more than five times reduced for both BBHs and BNSs.

VI. DISCUSSION

In our analysis, the coalescence time and the phase at the coalescence time for the nontensorial mode are assumed to be those of the tensor mode. If these parameters of the nontensorial modes are introduced to the polarization models, it may affect the estimation errors. We have checked how the modification of the coalescence time and the phase at coalescence affect the results by 1) changing the fiducial values of those parameters and 2) introducing another set of those parameters for a nontensorial mode. However, both 1 and 2 did not affect the final result of parameter estimation much. We also changed

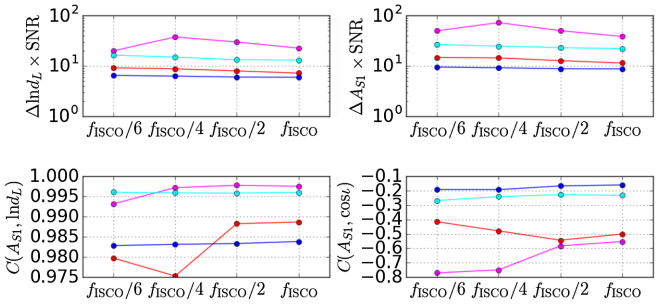

FIG. 4. The vertical axes are the estimation errors multiplied by the SNR and the correlation coefficients in the case of model TS1, and the horizontal one is the upper-frequency end used in evaluating the parameter estimation by Fisher analysis. The colors are $10\ M_\odot - 10\ M_\odot$ with HLV (magenta), $10\ M_\odot - 10\ M_\odot$ with HLVK (red), $1.4\ M_\odot - 1.4\ M_\odot$ with HLV (cyan), and $1.4\ M_\odot - 1.4\ M_\odot$ with HLVK (blue).

all the detector sensitivity by a factor of 10. The errors of the amplitude parameters in models TS1 and TS2 with HLV were reduced, but the errors in models TVsS2, TVyS1, and TV were not reduced with HLV because of the degeneracy among polarization modes. These indicate the polarization d.o.f. are characterized by overall amplitude parameters and require the same number of detectors to separate the modes and extract the polarization information from the detector signal of GWs in principle.

Figure 4 shows the maximum-frequency dependence of the errors in model TS1. We change the $f_{\rm max}$ to $f_{\rm ISCO}/2$, $f_{\rm ISCO}/4$, and $f_{\rm ISCO}/6$ and plot the errors multiplied by the SNR and correlation coefficients. For most cases, a change of $f_{\rm max}$ does not affect the amplitude estimation corrected by the SNR because the errors of the scalar-mode amplitude multiplied by the SNR are almost flat. This indicates that the change of $f_{\rm max}$ simply scales the amplitude error as well as the SNR. The exceptions, especially correlations in the case of $f_{\rm ISCO}/6 \simeq 35$ Hz and $f_{\rm ISCO}/4 \simeq 52$ Hz for BBHs, would appear due to the short integration range compared to $f_{\rm min} = 30$ Hz.

The additional polarization amplitudes correlate with the inclination angle strongly as shown in Table I. Figure 5 is the scatter plots of the errors of the nontensorial mode amplitudes vs the error of the inclination angle for BNSs in model TVxS2. It is shown that the different polarization modes depend on the inclination angle differently. Figure 6 is a scatter plot of A_{V_x} vs the inclination angle for BNSs in model TV. The plots of A_{V_x} in Figs. 5 and 6 show that the same polarization mode depends on the inclination angle the same way even in different models. We have checked that A_{V_y} in both models TVyS1 and TV behaves the same way and the scalar modes A_{S_1} and A_{S_2} also behave the same way in the different models. Figure 7 is the scatter plots of the errors of the nontensorial polarization amplitude A_{S_2} vs the estimation error of the inclination angle in model TS2 for BBHs and BNSs. In both cases of BBHs and BNSs, the distributions of the plots have the same appearance.

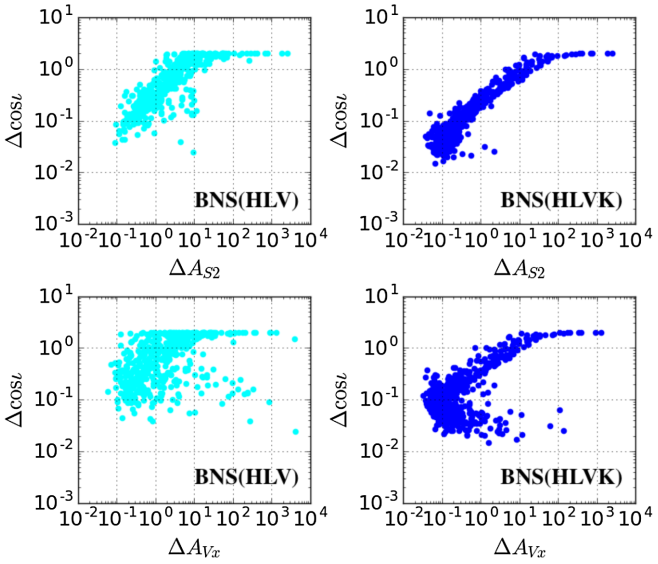

FIG. 5. Scatter plots of the error of the nontensorial polarization amplitudes vs the estimation error of the inclination angle for BNSs in model TVxS2. The colors are 1.4 $M_\odot$ − 1.4 $M_\odot$ with HLV (cyan) and 1.4 $M_\odot$ − 1.4 $M_\odot$ with HLVK (blue).

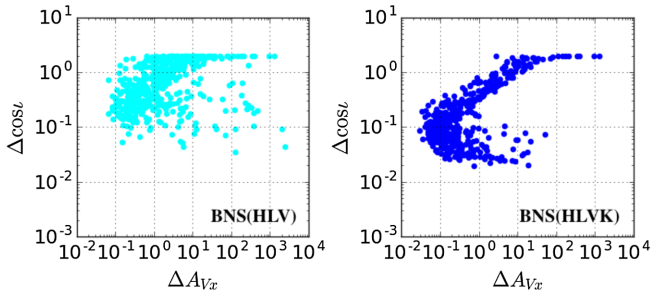

FIG. 6. Scatter plots of the error of the nontensorial polarization amplitude A_{V_x} vs the estimation error of the inclination angle for BNSs in model TV. The colors are 1.4 $M_\odot$ − 1.4 $M_\odot$ with HLV (cyan) and 1.4 $M_\odot$ − 1.4 $M_\odot$ with HLVK (blue).

We assume that the fiducial values of all the additional amplitude parameters for nontensorial modes are unity in our analysis above because we first need to understand the correlations between model parameters to reconstruct the polarization modes from the detector signal. We changed the fiducial values to 1/1000, 1/100, and 1/10 to show how the choice of the fiducial values affect the estimation errors. Figure 8 is the fiducial value dependence of the errors and correlation coefficients in model TS1. Since the error of the luminosity distance and the sky localization error are hardly changed, it indicates that the errors are mainly determined by the tensor modes. Also, the A_{S_1} error is hardly changed at the lower fiducial values than 1/10. It implies that the detection limit of the A_{S_1} is given roughly by 1/SNR. The correlation coefficients $C(A_{S_1}, \ln d_L)$ and $C(A_{S_1}, \cos\iota)$ are smaller for the smaller fiducial values. This also implies

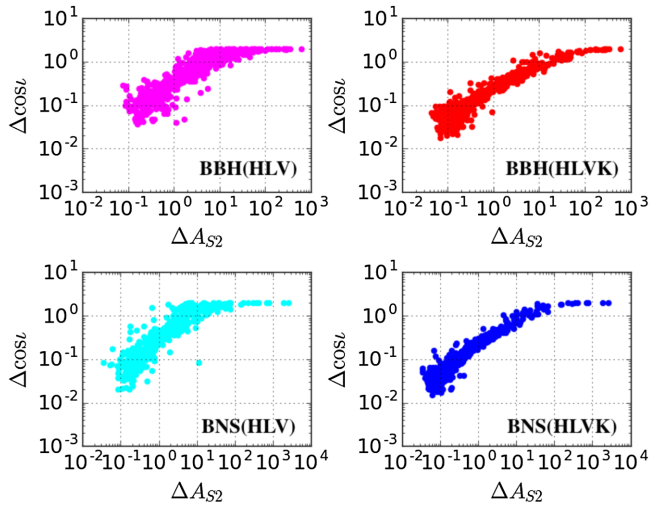

FIG. 7. A scatter plot of the error of the nontensorial polarization amplitudes vs the estimation error of the inclination angle in model TS2. The colors are 10 $M_\odot$ − 10 $M_\odot$ with HLV (magenta), 10 $M_\odot$ − 10 $M_\odot$ with HLVK (red), 1.4 $M_\odot$ − 1.4 $M_\odot$ with HLV (cyan), and 1.4 $M_\odot$ − 1.4 $M_\odot$ with HLVK (blue).

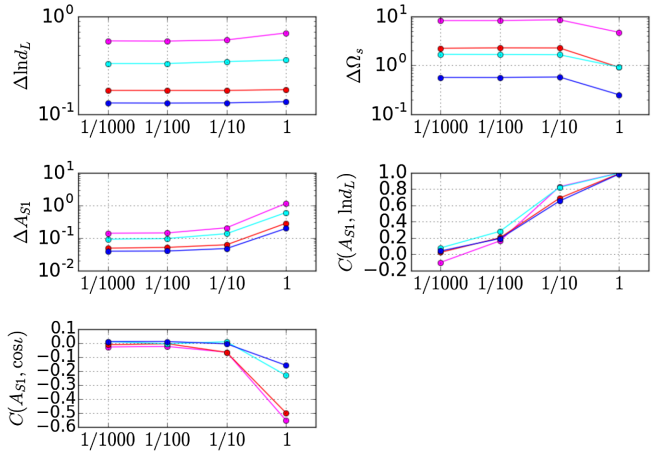

FIG. 8. The vertical axes are the estimation errors and the correlation coefficients in the case of model TS1, and the horizontal one is the fiducial values of the amplitude parameter A_{S_1} used in evaluating the parameter estimation by Fisher analysis. The colors are 10 $M_\odot$ − 10 $M_\odot$ with HLV (magenta), 10 $M_\odot$ − 10 $M_\odot$ with HLVK (red), 1.4 $M_\odot$ − 1.4 $M_\odot$ with HLV (cyan), and 1.4 $M_\odot$ − 1.4 $M_\odot$ with HLVK (blue).

that it is difficult to detect the A_{S_1} under the detection limit.

We also checked how the fiducial values affect the estimation errors in the other models TS2, TVxS2, TVyS1, and TV. The behavior of the estimation errors and the correlation coefficients are the same as in model TS1. Under the detection limit, which is given roughly by 1/SNR, the errors of the additional amplitude parameters are hardly changed, and it is difficult to detect those parameters.

VII. CONCLUSION

We estimated model parameters of the gravitational waves from compact binary coalescences with detector networks such as aLIGO-AdV(HLV) or aLIGO-AdV-KAGRA(HLVK) for various polarization models in which the polarization d.o.f. are characterized by overall amplitude parameters. We found that in principle at least the same number of detectors is required to separate the modes and extract the polarization information from the detector signal of gravitational waves. However, even if the number of detectors is equal to the number of the polarization modes, it is difficult to separate the modes in some cases, depending on the correlation among the amplitude parameters. Thereby, there are two conditions for the separation of polarization modes: (i) the same number of detectors as or more than the number of polarization modes and (ii) a significant SNR and the long duration of the signal. In general, there is a strong correlation between the additional polarization amplitude and the inclination angle of the binary orbit. For the same polarization modes, the appearance and strength of the correlation between the additional polarization amplitude and the inclination angle are the same even in different models as long as a degeneracy among the amplitude parameters is broken.

The participation of the fourth detector in the network of the gravitational-wave detectors will make it possible to extract the polarization information from the detector signal of the gravitational waves generated by the compact binary coalescences even in the case of the presence of two nontensorial polarizations in addition to tensor modes. In some cases with only one nontensorial polarization in addition to tensor modes, the separation of polarization modes is made possible with a fourth detector by breaking a parameter degeneracy.

ACKNOWLEDGMENTS

We thank C. P. Ooi for editing this article. H. T. and K. K. acknowledge financial support received from the Advanced Leading Graduate Course for Photon Science program at the University of Tokyo. H. T. is also supported by JSPS KAKENHI Grant No. 18J21016. A. N. was supported by JSPS KAKENHI Grant No. JP17H06358. K. N. is supported by JSPS KAKENHI Grant No. 17J01176. This work was supported by JSPS Grant-in-Aid for Scientific Research (B), Grant No. 18H01224. This study was supported by MEXT, JSPS Leading-edge Research Infrastructure Program, Grant-in-Aid for Scientific Research on Innovative areas (Grants No. 2905, No. 17H06357, and No. 17H06365). This work was supported by MEXT, JSPS Leading-edge Research Infrastructure Program, JSPS Grant-in-Aid for Specially Promoted Research 26000005, MEXT Grant-in-Aid for Scientific Research on Innovative Areas 24103005, JSPS Core-to-Core Program, A. Advanced Research Networks, the joint research program of the Institute for Cosmic Ray Research, University of Tokyo, National Research Foundation and Computing Infrastructure Project of KISTI-GSDC in Korea, the LIGO project, and the Virgo project.

[1] J. Aasi *et al.* (The LIGO Scientific Collaboration), Classical Quantum Gravity **32**, 074001 (2015).
[2] B. P. Abbott *et al.*, Phys. Rev. Lett. **116**, 061102 (2016).
[3] F. Acernese *et al.*, Classical Quantum Gravity **32**, 024001 (2015).
[4] B. P. Abbott *et al.*, Phys. Rev. X **6**, 041015 (2016).
[5] B. P. Abbott *et al.*, Phys. Rev. Lett. **119**, 161101 (2017).
[6] E. Newman and R. Penrose, J. Math. Phys. (N.Y.) **3**, 566 (1962).
[7] M. E. S. Alves, O. D. Miranda, and J. C. N. de Araujo, Classical Quantum Gravity **27**, 145010 (2010).
[8] D. M. Eardley, D. L. Lee, A. P. Lightman, R. V. Wagoner, and C. M. Will, Phys. Rev. Lett. **30**, 884 (1973).
[9] C. M. Will, *Theory and Experiment in Gravitational Physics* (Cambridge University Press, Cambridge, England, 1993).
[10] C. Brans and R. H. Dicke, Phys. Rev. **124**, 925 (1961).
[11] A. De Felice and S. Tsujikawa, Living Rev. Relativity **13**, 3 (2010).
[12] M. Visser [arXiv:gr-qc/9705051 (General Relativ. Gravit.)].
[13] V. A. Rubakov and P. G. Tinyakov, Phys. Usp. **51**, 759 (2008).
[14] K. Somiya, Classical Quantum Gravity **29**, 124007 (2012).
[15] Y. Aso, Y. Michimura, K. Somiya, M. Ando, O. Miyakawa, T. Sekiguchi, D. Tatsumi, and H. Yamamoto, Phys. Rev. D **88**, 043007 (2013).
[16] T. Akutsu *et al.*, Prog. Theor. Exp. Phys. **2018**, 013F01 (2018).
[17] KAGRA Collaboration, arXiv:1710.04823.
[18] K. Hayama and A. Nishizawa, Phys. Rev. D **87**, 062003 (2013).
[19] A. Nishizawa, A. Taruya, K. Hayama, S. Kawamura, and M.-a. Sakagami, Phys. Rev. D **79**, 082002 (2009).
[20] M. Isi, A. J. Weinstein, C. Mead, and M. Pitkin, Phys. Rev. D **91**, 082002 (2015).
[21] M. Isi and A. J. Weinstein, arXiv:1710.03794.
[22] A. A. Svidzinsky, arXiv:1712.07181.
[23] B. P. Abbott *et al.*, Phys. Rev. Lett. **119**, 141101 (2017).
[24] M. E. Tobar, T. Suzuki, and K. Kuroda, Phys. Rev. D **59**, 102002 (1999).

[25] J. D. E. Creighton and W. G. Anderson, *Gravitational-Wave Physics and Astronomy* (Wiley-VCH, Weinheim, Germany, 2011).
[26] E. Berti, A. Buonanno, and C. M. Will, Phys. Rev. D **71**, 084025 (2005).
[27] M. Maggiore, *Gravitational Waves* (Oxford University, New York, 2007).
[28] K. Chatziioannou, N. Yunes, and N. Cornish, Phys. Rev. D **86**, 022004 (2012).
[29] L. S. Finn, Phys. Rev. D **46**, 5236 (1992).
[30] C. Cutler and É. E. Flanagan, Phys. Rev. D **49**, 2658 (1994).
[31] S. Khan, S. Husa, M. Hannam, F. Ohme, M. Pürrer, X. J. Forteza, and A. Bohé, Phys. Rev. D **93**, 044007 (2016).
[32] B. P. Abbott *et al.*, Living Rev. Relativity **19**, 1 (2016).